

Article

Integration of Computational Fluid Dynamics and Artificial Neural Network for Optimization Design of Battery Thermal Management System

Ao Li ¹, Anthony Chun Yin Yuen ^{1,*}, Wei Wang ¹, Timothy Bo Yuan Chen ¹, Chun Sing Lai ², Wei Yang ³, Wei Wu ⁴, Qing Nian Chan ¹, Sanghoon Kook ¹ and Guan Heng Yeoh ¹

- ¹ School of Mechanical and Manufacturing Engineering, University of New South Wales, Sydney, NSW 2052, Australia; ao.li@unsw.edu.au (A.L.); wei.wang15@unsw.edu.au (W.W.); timothy.chen@unsw.edu.au (T.B.Y.C.); qing.chan@unsw.edu.au (Q.N.C.); s.kook@unsw.edu.au (S.K.); g.yeoh@unsw.edu.au (G.H.Y.)
- ² Brunel Interdisciplinary Power Systems Research Centre, Department of Electronic and Electrical Engineering, Brunel University London, Kingston Lane, London UB8 3PH, UK; chunsing.lai@brunel.ac.uk
- ³ School of Energy, Materials and Chemical Engineering, Hefei University, 99 Jinxiu Avenue, Hefei 230601, China; yangwei@hfuu.edu.cn
- ⁴ Department Materials Science and Engineering, City University of Hong Kong, Tat Chee Avenue, Hong Kong 999077, China; weiwu39-c@my.cityu.edu.hk
- * Correspondence: c.y.yuen@unsw.edu.au; Tel.: +61-2-9385-5697



Citation: Li, A.; Yuen, A.C.Y.; Wang, W.; Chen, T.B.Y.; Lai, C.S.; Yang, W.; Wu, W.; Chan, Q.N.; Kook, S.; Yeoh, G.H. Integration of Computational Fluid Dynamics and Artificial Neural Network for Optimization Design of Battery Thermal Management System. *Batteries* **2022**, *8*, 69. <https://doi.org/10.3390/batteries8070069>

Academic Editors: Carlos Ziebert and Pascal Venet

Received: 7 June 2022

Accepted: 7 July 2022

Published: 8 July 2022

Publisher's Note: MDPI stays neutral with regard to jurisdictional claims in published maps and institutional affiliations.



Copyright: © 2022 by the authors. Licensee MDPI, Basel, Switzerland. This article is an open access article distributed under the terms and conditions of the Creative Commons Attribution (CC BY) license (<https://creativecommons.org/licenses/by/4.0/>).

Abstract: The increasing popularity of lithium-ion battery systems, particularly in electric vehicles and energy storage systems, has gained broad research interest regarding performance optimization, thermal stability, and fire safety. To enhance the battery thermal management system, a comprehensive investigation of the thermal behaviour and heat exchange process of battery systems is paramount. In this paper, a three-dimensional electro-thermal model coupled with fluid dynamics module was developed to comprehensively analyze the temperature distribution of battery packs and the heat carried away. The computational fluid dynamics (CFD) simulation results of the lumped battery model were validated and verified by considering natural ventilation speed and ambient temperature. In the artificial neural networks (ANN) model, the multilayer perceptron was applied to train the numerical outputs and optimal design of the battery setup, achieving a 1.9% decrease in maximum temperature and a 4.5% drop in temperature difference. The simulation results provide a practical compromise in optimizing the battery configuration and cooling efficiency, balancing the layout of the battery system, and safety performance. The present modelling framework demonstrates an innovative approach to utilizing high-fidelity electro-thermal/CFD numerical inputs for ANN optimization, potentially enhancing the state-of-art thermal management and reducing the risks of thermal runaway and fire outbreaks.

Keywords: thermal management; lithium-ion batteries; CFD modelling; ANN; optimization design

1. Introduction

With recent advancements in electric technology as well as the growing global concern of energy crisis and environmental pollution, a lot of research interests are devoted to the search for alternative energy sources, including nuclear, wind, or solar energy. Battery energy storage systems have caught the public eye due to their many advantages: fast responsiveness, controllability, structural independence, and widespread application range [1]. Lithium-ion based battery energy storage systems have become the most competitive choice for various applications [2–5]. Lithium-ion batteries (LIBs) as a source of alternative energy through renewable energies have been proposed in industries for many portable consumer electronic devices, including cell phones and laptops. Moreover, LIBs have begun to enter the automotive market as power packs for hybrid and battery electric

vehicles (HEVs and EVs) due to their enormous power, efficiency, and durability of a charge cycle.

Temperature plays a critical role in many aspects of the performance of LIBs, including charge acceptance [6], energy capability [7], reliability [8], and so on. In comparison with other battery technologies, LIB performs relatively poor thermal stability, and many accidents happened in recent years [9–11]. A typical LIB comprises four main components: an anode, a cathode, a separator, and an electrolyte. All the parts form a closed system separated from the air, so there is no explosion or fire danger at the normal working temperature [12]. However, the abuse of LIB will generate the threat of thermal runaway and overheating. Both positive and negative electrode decomposition are exothermic processes. Also, oxygen can be generated during the decomposition reactions. The generated heat and oxygen are the contributions to the combustion triangle. If the battery experiences harsh working conditions during electric transportation, the generated heat triggers electrodes' decomposition. As a result, the battery potentially faces thermal issues. Suppose the cell temperature is rising over a certain threshold. In that case, a thermal runaway may turn up, leading to a quick temperature rise and potentially other related undesirable consequences such as the generation of toxic gas and smoke. With the rising battery temperature over a critical point, the other chain exothermic reactions happen. The temperature and pressure in the LIB are cumulated until it exceeds the battery endurance. Eventually, the fire and rupture/explosion are inescapable. Therefore, the thermal management of LIB is essential during the battery working process or battery application. It is also crucial to investigate the LIB thermal runaway process by accurately monitoring and predicting temperature dynamics during thermal propagation and implementing functional methods to improve the cooling efficiency of the battery itself and the battery system.

There are two key topics of concern in battery thermal management: handling the charge/discharge cycle and governing the battery heat growth [13,14]. Many pieces of research focused on the battery thermal management system of EVs have been conducted [15–17]. The heat produced during the operating process has been established as the major rise in the working temperature. Computation Fluid Dynamics (CFD) is a practical tool for investigating thermal properties and simulating multiple physics fields [18]. CFD simulations could provide detailed information about the electrical and thermal areas inside the battery during the work process that is often challenging to assess and extract by experimental approaches. Model-based investigations promote a theoretical and comprehensive understanding of battery physics beyond what is possible from practical methods only. For example, Kirad and Chaudhari [19] applied numerical models for studying the selection of the battery module spacing with an improvement in cooling performance. Due to the development of computing capability, numerical simulations are gradually applied in battery models, battery components and materials studies, and battery safety engineering [20–22]. Most numerical studies rely on the thermal models, which predict the average surface temperature for a LIB cell [23–26], and lots of experimental investigations on thermal propagation have been carried out [27–30]. Nevertheless, to achieve a proper estimation of the thermal behaviour of a battery, many aspects, including the shape, layout, and physical and electrochemical properties, should be illustrated as closely as possible in the simulation. For instance, the asymmetric surface temperature of a battery cell should be considered in the model. The non-uniform temperature distribution in the LIBs leads to an electrical imbalance, lower battery performance, and shorter battery life [31,32]. Regarding the detailed temperature distribution, an electric-thermal model with the non-uniform feature should be built.

Moreover, battery thermal management systems have been classified in various ways based on different criteria [33–35]. For example, battery thermal management systems can be branched into three kinds based on various mediums: air-based, liquid-based, and phase change materials-based. Several optimization studies on the battery thermal management system have been previously conducted [36–39]. The air-cooling method is considered the most traditional approach and is a favoured option for HEVs and EVs. It is clear that the optimization of battery packs or systems depends on many parameters, such as geometry

structure, coolant properties, operating conditions, and so force. Still, few researchers focus on multiple parameters simultaneously.

As a part of artificial intelligence, machine learning focuses on the study of accuracy improvement by computer algorithms and data to imitate how humans learn [40,41]. The application of machine learning techniques, particularly artificial neural networks (ANN), can be a potential method to optimize the battery system. Because LIBs are highly complex, nonlinear systems, applying a probabilistic approach allows for quantification of uncertainty, which positively impacts making decisions in design and control. ANN model is a kind of model that characterizes the interrelation between inputs and outputs by using a collection of interconnected nodes (perceptron). The application of ANN to battery research is still relatively new. Wu et al. [42] generated a design map that fulfills both specific energy and specific power requirements using a systematic approach based on ANN. Qian et al. [43] optimized the battery spacing by neural network model and demonstrated the interrelationship between layout and temperature of battery packs. Feng et al. [44] developed an electrochemical-thermal-neural-network method used for the co-estimation of LIB state of charge (SOC) and state of temperature. Shi et al. [45] applied the fully connected deep network approach to study air-based cooling LiFePO₄ cuboid battery packs and optimize the U-type structure. However, pioneering studies have highlighted the possibility of using ANN for battery thermal problems. These studies include modelling battery spacing, specific format, and some battery performances. The detailed temperature distribution of LIB and battery pack have not been fully investigated. Besides, the ambient temperature and natural ventilation should be considered during the battery working process. Therefore, the combination between ANN analysis and the electro-thermal battery model is proposed to investigate further the battery system's cooling efficiency and battery fire safety performance. Figure 1 shows the schematic figure of the integrated CFD-ANN model proposed in this study.

Numerical tool coupling ANN trained multilayered parameter inputs with thermal analysis for battery performance and optimum configuration design

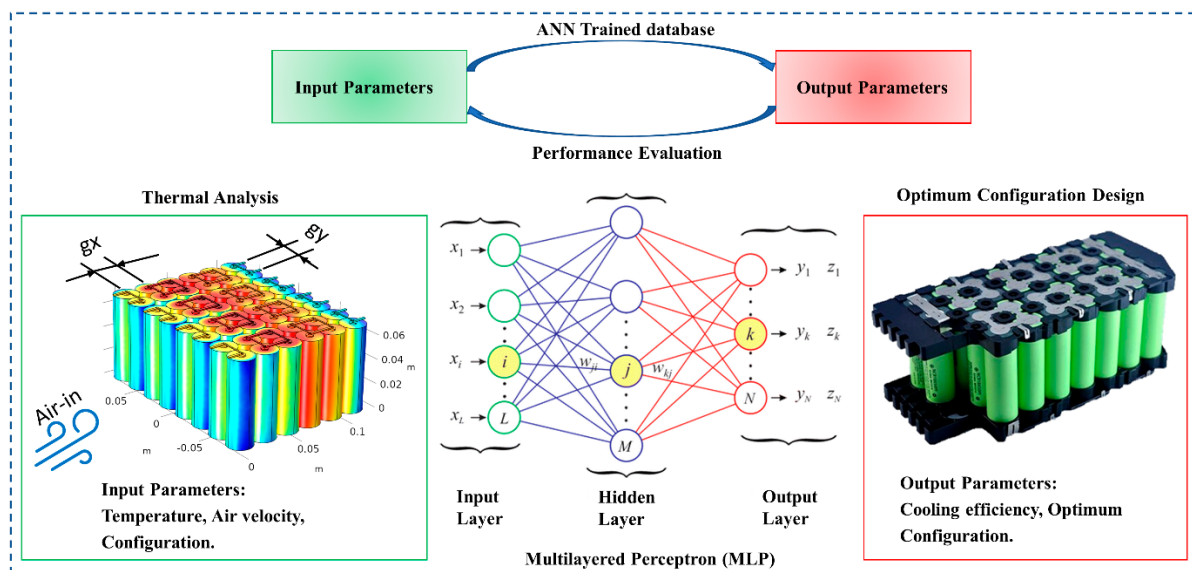


Figure 1. Schematic of the proposed CFD-ANN model.

To this end, the non-uniform distributions of the battery cell should be investigated for the thermal analysis, which can be treated as a measurement and prediction at the early stage of the Li-ion battery thermal runaway fires. Furthermore, with the numerical analysis, a better understanding of battery pack configuration design can be achieved. In this article, the contributions are:

- (i) Establishment and development of a three-dimensional electro-thermal model capable of considering temperature distribution of battery packs and heat exchange with the ambient environment.
- (ii) Utilize the numerical results to comprehensively describe and predict the battery system's thermal behaviour to improve battery safety during the designing and working stages.
- (iii) Coupled the electro-thermal model with the ANN model to optimize the battery system configuration design and enhance the cooling performance of the battery system.

The outline of this paper is summarized as follows: Section 2 introduces the numerical models applied in this paper, including electrochemical model, thermal model, and ANN model. Section 3 demonstrates the numerical results of the proposed model with validation and verification. Also, the training process and optimization results are listed in this section. Finally, the author presented some conclusions and proposed the future perspectives on this field in the conclusion section.

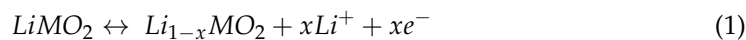
2. Numerical Models Applied in the Battery Pack

2.1. Electrochemical Model

The electrochemical model applied in this study could be seen as a lumped version of a single particle model [46], simulating the transport of intercalated lithium in one of the electrodes. The single particle model predicts the temperature distribution and voltage changes in a single LIB cell during galvanostatic operations. The simplification of this model can be conducted when the battery is mainly controlled by the diffusion process in one of the electrodes only. The model is based on a complete model of a LIB working process cycle [47]. In this model, the lumped battery interfaces are utilized, and the battery cell voltage E_{cell} is calculated by applying time-dependent cell current I_{cell} . Additionally, the battery open circuit voltage data, named E_{OCV} , is estimated from SOC.

The three-dimensional electro-thermal model built in this paper is based on a typical cylindrical LiFePO₄/Carbon power battery, considering the physical and electrical conservations, as well as thermal principles and electrochemical kinetics. The electrochemical reactions of common LIBs can be described as the following Equations (1)–(3), where M stands for a metal, which is used as a cathode material such as cobalt or nickel, and C is recognized as the anode materials.

The reaction at the positive electrode is described as:



The chemical reaction at the negative electrode is expressed as:



The overall reaction can be presented as:

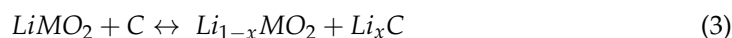


Figure 2 demonstrates the working process of a typical LIB, and the fundamental cell unit is considered a sandwich structure, including the positive electrode, the separator, the negative electrode, and the current collectors located at both electrodes. The metal tab is joined at each correlated current collector and electrode. The separator is located between cathode and anode, a porous polymer membrane to prevent physical contact of electrodes. The electrolyte is the medium that enables the ion transport mechanism between electrodes. It requires specific working conditions, such as significant ion conductivity, low-set electrical conductivity, extended temperature range of operation, thermo-dynamically stable at a certain range of voltages, environmentally friendly, etc.

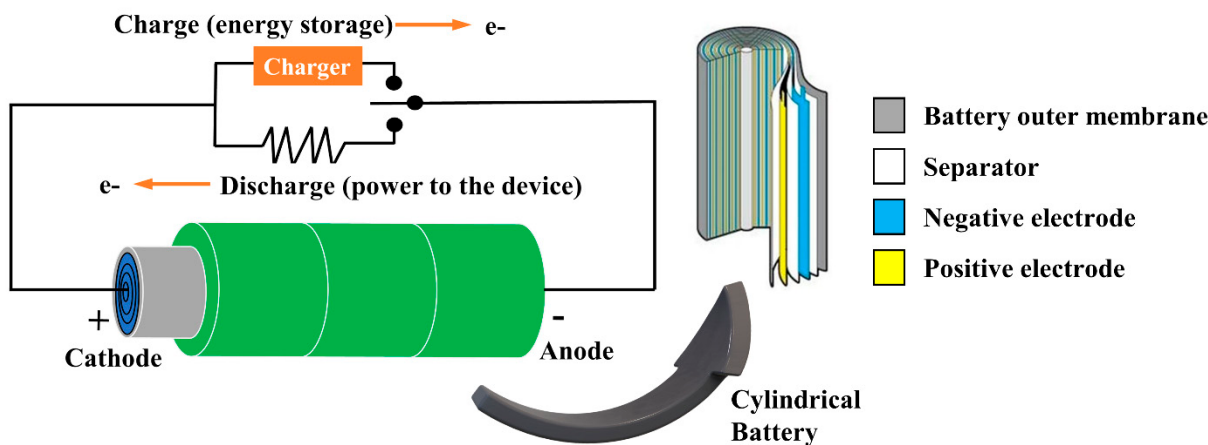


Figure 2. The principle of operation for a typical LIB and its structure.

Each electrode and separator is impregnated with electrolyte, achieving transportation of lithium ions. The material parameters for the electrolyte refer to a plasticized ethylene carbonate/dimethyl carbonate (EC/DMC) electrolyte remaining in a polymer matrix. Therefore, the stated electrolyte volume fraction points to this model's total liquid electrolyte and polymer matrix volume fractions. In this model, the potential losses η_{IR} due to ohmic and charge transfer processes are given as follows:

$$\eta_{IR} = \eta_{IR,1C} \frac{I_{cell}}{I_{1C}} \quad (4)$$

where $\eta_{IR,1C}$ represents the potential losses under the 1C current. The 1C current I_{1C} means that the discharge current will discharge the entire battery in one hour, and it is calculated as:

$$I_{1C} = \frac{Q_{cell,0}}{3600 \text{ s}} \quad (5)$$

The dimensionless charge exchange current J_0 is applied for the integrated voltage dissipation accompanied by the charge delivery reactions on the two electrodes' surfaces, shown as:

$$\eta_{act} = \frac{2RT}{F} \operatorname{asinh} \left(\frac{I_{cell}}{2J_0 I_{1C}} \right) \quad (6)$$

The diffusion processes also lead to potential loss, which is represented by η_{act} . Derived from diffusion in an idealized particle or by applying a resistor-capacitor combination, concentration overpotential effects can be explained among the lumped battery interfaces. In this model, particle diffusion is calculated. Fickian diffusion of a dimensionless SOC parameter is calculated in this case, using spherical symmetry, according to:

$$\tau \frac{\partial SOC}{\partial t} = -\nabla \cdot (-\nabla SOC) \quad (7)$$

The interval stands for a common particle of the electrode controlling the cell, where $X = 0$ and $X = 1$ mean the particle centre and particle surface accordingly.

The operating conditions at the particle boundary are as follows:

$$\nabla SOC = 0|_{X=0} \quad (8)$$

$$\nabla SOC = \frac{\tau I_{cell}}{N_{shape} Q_{cell,0}} \Big|_{X=1} \quad (9)$$

where N_{shape} equals three for spherical particles in this model. The SOC of the surface, $SOC_{surface}$, is identified at the particle surface. The average SOC, named $SOC_{average}$, is

prescribed by lumping the particle volume, appropriately considering spherical coordinates, and is defined as:

$$SOC_{average} = \frac{\int_0^1 SOC 4 \prod X^2 dX}{\int_0^1 4 \prod X^2 dX} = 3 \int_0^1 SOC X^2 dX \quad (10)$$

The integrated voltage dissipation accompanied by concentration overpotential is represented by η_{conc} and defined as:

$$\eta_{conc} = E_{ocv}(SOC_{surface}) - E_{ocv}(SOC_{average}) \quad (11)$$

Lastly, the battery cell voltage E_{cell} is defined as:

$$E_{cell} = E_{ocv}(SOC_{average}) + \eta_{IR} + \eta_{act} + \eta_{conc} \quad (12)$$

Establishing the explanation of η_{conc} and E_{cell} is also calculated as:

$$E_{cell} = E_{ocv}(SOC_{surface}) + \eta_{IR} + \eta_{act} \quad (13)$$

The battery model involves these three steps. At first, a lumped battery model is set up and run for a time-dependent battery current. Then, parameter estimation of the parameters $\eta_{IR,1C}$, τ , and J_0 is demonstrated using experimental data. This is achieved using the Global Least-Squares Objective node in the optimization interface, combined with the optimization study step using a Levenberg-Marquardt optimization solver. Lastly, cell voltage prediction is performed using the optimized lumped parameter values obtained in the previous parameter estimation study compared with experimental data.

2.2. Thermal Model

In this study, the thermal model is based on a previous two-dimensional axial symmetry approach, simulated by the Heat Transfer in Solids module. A spirally wound type of battery is chosen for this simulation, and the simplification of the heat conduction can be achieved along the spiral direction. Moreover, instead of simulating the heat conduction in each layer along the radial direction, the wound sheets are acted as a combination cell material domain. These approximations are understandable for spiral wound battery cells cooled under natural convection. The model configuration comprises three connection sections: (1) Battery outer can; (2) A combination cell material domain; (3) Center axis (mandrel where the battery cell sheets are wound).

For this model, several equations and parameters are considered. Considering the anisotropic thermal conductivities in this model and differences among various directions [48], the thermal conductivities along the radial path, $k_{T,r}$, and along the cylinder length direction, $k_{T,ang}$, are defined separately as follows:

$$k_{T,r} = \frac{\sum L_i}{\sum L_i / k_{T,i}} \quad (14)$$

$$k_{T,ang} = \frac{\sum L_i k_{T,i}}{\sum L_i} \quad (15)$$

The density ρ_{batt} and heat capacity $C_{p,batt}$ for the combination cell material domain is defined as stated by the following equations:

$$\rho_{batt} = \frac{\sum L_i \rho_i}{\sum L_i} \quad (16)$$

$$C_{p,batt} = \frac{\sum L_i C_{p,i}}{\sum L_i} \quad (17)$$

The heat source produced by the combination cell material domain is identified by employing the Electrochemical Heating Multiphysics coupling module. However, the heat source term in the combination cell material domain is scaled to solve the lack of heat generation in the current collectors and the canister thickness. This mounted heat source is acquired by multiplying two factors of the volumetric heat source from the 1D Li-ion battery model. The former factor is the fraction of the total 1D model in which heat is produced. That is the total length value of electrodes and the separator, divided by the total battery length, including the measurements of both current collectors. The latter factor is the fraction of the entire 3D cylindrical battery. The volume in which heat is produced is the cell's total volume, including the homogenized wound layers of the cell material, the centre axis, and the battery case, minus the volume of the outer case and the volume of the battery centre axis. This heat source is then divided by the total volume of the battery cell domain, which is the difference between the whole battery volume and the centre axis volume. Thereby, the following equation for the 3D heat source is demonstrated:

$$Q_{h,3D} = Q_{h,1D} \frac{L_{neg} + L_{sep} + L_{pos}}{L_{batt}} \frac{((r_{batt} - d_{can})^2 - r_{mandrel}^2)(h_{batt} - 2d_{can})}{(r_{batt}^2 - r_{mandrel}^2)h_{batt}} \quad (18)$$

For the lumped battery interface model, Arrhenius expression is applied to model each battery cylinder, with temperature-dependent ohmic, exchange current, and diffusion time-constant parameters.

The thermal conductivity in the combination cell material domain is anisotropic due to the spiral type of the battery. The orthotropic thermal conductivity in the combination cell material domain is solved by introducing a cylindrical coordinate system in the model. The zero-Mach-number limit of the compressible conservation equations was applied to depict the flow movement and heat transfer. Regarding the enthalpy equation and the temperature equation, the energy conservation for incompressible fluid can be simplified to:

$$\rho C_p \frac{\partial T}{\partial t} + \rho C_p \mathbf{v} \cdot \nabla T = \nabla \cdot (k \nabla T) + Q \quad (19)$$

2.3. ANN Model

ANN has rapidly developed in recent decades as a common tool to model a broad range of engineering systems due to its capability to learn and adapt to find potential correlations among different properties, mainly to map the nonlinear relationship of inputs and outputs. A hidden layer is a layer located between the input and output of the ANN model, in which artificial neurons applies a set of weights to the inputs and directs them through an activation function as the output. Hidden layers of ANN allow for a neural network's function to be taken apart for specific data transformations. For example, images and documents are treated as initial inputs from external data. The ultimate outcomes complete the task, such as recognizing objects in a snap.

A typical ANN model compromises five main components: inputs, summation functions, weights, activation functions, and outputs. The artificial neuron in the hidden layer works as a biological neuron in the brain. To form a directed, weighted graph, the network is formed by linking the output of specific neurons to the input of other neurons. A learning process can adapt the activation functions and weights. The learning rule or training approach controls the certain learning process. The summation function (denoted by E) is a function that calculates the net inputs, considering adjustable weights w_{ij} and bias w_{bi} , expressed as:

$$E = \sum_{j=1}^n w_{ij}x_j + w_{bi} \quad (20)$$

The activation function of a node governs the output of that node, or “neuron,” provided input or set of inputs. The activation function presents a functional relationship between the input and output layers. Some frequently applied activation functions are step

activation, threshold function, sigmoid function, and hyperbolic tangent function [49]. The logistics sigmoid function is adopted in this study and is presented as:

$$f(E) = \frac{1}{1 + e^{-E}} \quad (21)$$

The number of hidden neurons determined by the formulation according to neural network design [50] is given by:

$$N_h = \frac{N_s}{(\alpha(N_i + N_o))} \quad (22)$$

where the subscripts h denotes the number of input neurons, s is the sample amount in the training dataset, o is the number of outputs, and α is a scaling factor ranging from 2–10. In this study, α is prescribed as 2 to achieve an optimal solution without overfitting, and ten hidden neurons were applied in the ANN model.

3. Results and Discussions

3.1. Electro-Thermal Model Simulation Results

In this paper, a corporate software applied finite element, COMSOL Multiphysics 5.5, was employed to study the three-dimensional electro-thermal coupled model. The default mesh component was applied for generating the mesh, and mesh independence was examined as well. The MUMPS time-dependent solver was applied for battery variables, and the PARDISO solver was chosen for heat transfer variables. The mesh applied for this study consists of triangular and quadrilateral elements developed by COMSOL Multiphysics 5.5. In order to obtain the thermal behaviour and boundary layer spread, the refined mesh is achieved at the connections of the battery boundary. Mesh independence verification was performed to avoid the grid number and mesh quality impact on the simulation results, shown in Table 1. According to Table 1, 43,486 elements show reliable and efficient results, and more elements lead to larger computation time. Therefore, the total number of meshes is about 43,486 elements chosen for the validation case, considering the efficiency and accuracy. For the battery pack simulation, the most appropriate grid amount is around 211,907 elements. Subsequently, more simulation results are produced to feed the machine learning model to training.

Table 1. This is a table. Tables should be placed in the main text near to the first time they are cited.

Grid Resolution	Elements Number	Calculation Time	Maximum Electrolyte Temperature
Finer	114,273	75.6 min	20.250 °C
Fine	43,486	30.5 min	19.829 °C
Normal	23,986	18.7 min	19.810 °C
Coarse	9708	10.6 min	18.910 °C

The validation of the electrochemical model and thermal model is established on the Type 38,120 battery cell, in which the nominal voltage is 3.2 V and capacity is 10 Ah, as well as the thickness of the cathode, the separator, and the anode are 91 µm, 40 µm and 142 µm, respectively. The type we choose is one of the most commonly used in the current commercial market. It is developed based on physical and electrical conservations, as well as thermal principles and electrochemical kinetics. The battery pack investigation for the three-dimensional electro-thermal model is built by Type 21,700 battery cylinders with a nominal capacity of 4 Ah and a nominal voltage of 3.6 V. The battery pack is constructed by coupling two cylindrical batteries in parallel. Then the mated battery pairs are connected in series. The geometry and battery parameters are listed in Table 2. The geometry specifications are used to build the battery domain for thermal simulations, while the battery parameters are applied for the simulation of the electrochemical model.

Table 2. Geometry dimension and electrochemical parameters of the battery cell.

Geometry Parameters			Battery Parameters		
d_batt	21 [mm]	Battery diameter	C_rate	4	C rate
			Q_cell	4 [A·h]	Battery cell capacity
r_batt	d_batt/2	Battery radius	I_1C	Q_cell/1 [h]	1C current
h_batt	70 [mm]	Battery height	kT_batt_ang	30 [W m ⁻¹ K ⁻¹]	Thermal conductivity, in plane
			kT_batt_r	1 [W m ⁻¹ K ⁻¹]	Thermal conductivity, cross plane
h_term	1 [mm]	Terminal thickness	Ea_eta1C	24 [kJ mol ⁻¹]	Activation energy
			Ea_J0	-59 [kJ mol ⁻¹]	Activation energy
			Ea_Tau	24 [kJ mol ⁻¹]	Activation energy
r_term	3 [mm]	Terminal radius	T0	20 [°C]	Reference temperature
d_sc	2 [mm]	Serial connector depth	J0_0	0.85	J0 at reference temperature
h_sc	1 [mm]	Serial connector height	tau_0	1000 [s]	tau at reference temperature
			eta_1C	4.5 [mV]	eta_1C at reference temperature
h_pc	0.5 [mm]	Parallel connector height	rho_batt	2000 [kg m ⁻³]	Battery density
w_pc	1 [mm]	Parallel connector width	Cp_batt	1400 [J kg ⁻¹ K ⁻¹]	Battery heat capacity
			ht	30 [W m ⁻² K ⁻¹]	Heat transfer coefficient
			T_init	20 [°C]	Initial/external temperature

The initial battery state is fully charged. The discharge process at different current densities is simulated, and the discharge curves during the process are demonstrated. The battery capacity under various discharge rates is built through the modelling. The simulation will be stopped when the cell potential decreases under 3 V, which is the state of end-of discharge. The simulation result of the nominal discharge current density representing case 1C, is shown in Figure 3a. The numerical result shows a good agreement with the experiment data. Meanwhile, there are a few deviations in the usual discharge voltage plateau related to the thermodynamic analytics and battery prototypes. The thermal model is validated, and the results are shown in Figure 3b. The experimental data is extracted from the surface of the battery along the axis to track the surface temperature development. The simulation results in the same location of the testing point have similar growth trends. The slight difference between the experimental and numerical results is because of the temperature rise of the experiment due to the local ohmic heat generation, where the electrical contact resistance among the connectors and terminals of the battery.

Considering the electrochemical performance, the current flows inside the battery cell and battery pack remain similar due to applying a single particle model. The Single Particle Battery interface answers for solid diffusion in the electrode particles and the intercalation reaction kinetics. A lumped solution resistance term is used for covering the ohmic potential drop inside the electrolyte. The cell capacity is specified through fractional volumes of both electrodes in the battery. The individual electrode operational state-of-charges are used to identify the initial charge distribution in the battery. The temperature contour and heat flux streamline of the proposed battery pack shows the temperature distribution on the whole battery pack during its working process by the proposed electro-thermal model. The maximum temperature of the battery's innermost parts is around 2 °C higher than the outermost parts. It also provides the temperature difference of the whole battery pack. With the utilization of this lumped model, the broad temperature distribution of battery cell surfaces can be represented. Besides, the heat flux generated inside the battery cell can be simulated, as well as the heat exchange between battery surfaces and the ambient cooling air can be simulated numerically.

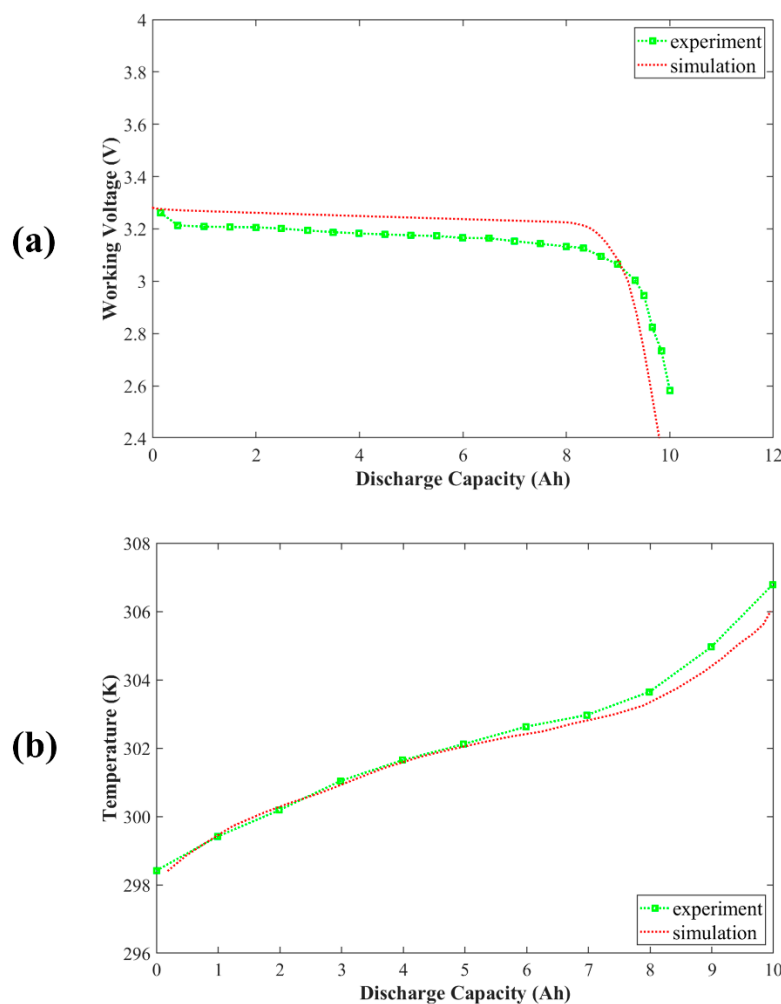


Figure 3. Comparison of numerical results of working voltage (a) and temperature (b) with experimental results [23] during 1C galvanostatic discharge under natural convection conditions.

Through the numerical study for the whole battery pack, the configuration setup of the battery pack is also investigated. The two-dimensional parameters are defined by different directions with various gaps, which are no gap (0 m), half of a cell (0.01 m) and one cell (0.02 m). Through permutation and combination, nine sets of collocations are formed. Figure 4 shows that all the battery cells are constructed together with various gap setups among the parallel-coupled battery pairs, which are the first nine cases. The gap enhances the convective and conductive between battery cells and ambient air from the battery safety perspective, improving battery pack cooling efficiency and fire safety.

To further understand the battery temperature distribution, air velocity and ambient environment are considered as well. Buoyancy forces cause natural convection as a consequence of density changes ascribed to temperature differences in the fluid. At heating, the fluid will rise because of the density variation in the boundary layer. Meanwhile, the cooler fluid, which will heat and increase, will replace the raised fluid. This continuous phenomenon is named free or natural convection. Thus, this study selected four sets of air velocity. Moreover, the temperature difference (The difference between the highest and the lowest temperature of the battery pack) and maximum temperature (The maximum temperature of a battery cell) are also considered. Figure 5 plots the maximum temperature and temperature difference profiles under various operating conditions, where the geometry conditions remain the same. From Figure 5a,c, air velocity positively impacts decreasing the maximum temperature and temperature difference. Under the same ambient temperature, shown in Figure 5b, increasing the air velocity can enhance the cooling efficiency, but the

drop in maximum temperature is not much. Figure 5c, cases with air velocity 4 m s^{-1} achieve 36%, which is the maximum percentage of temperature difference drop compared to other cases in this configuration. It is demonstrated that when the minimum values of maximum temperature and temperature difference are reached, the format set up is the best and optimization results.

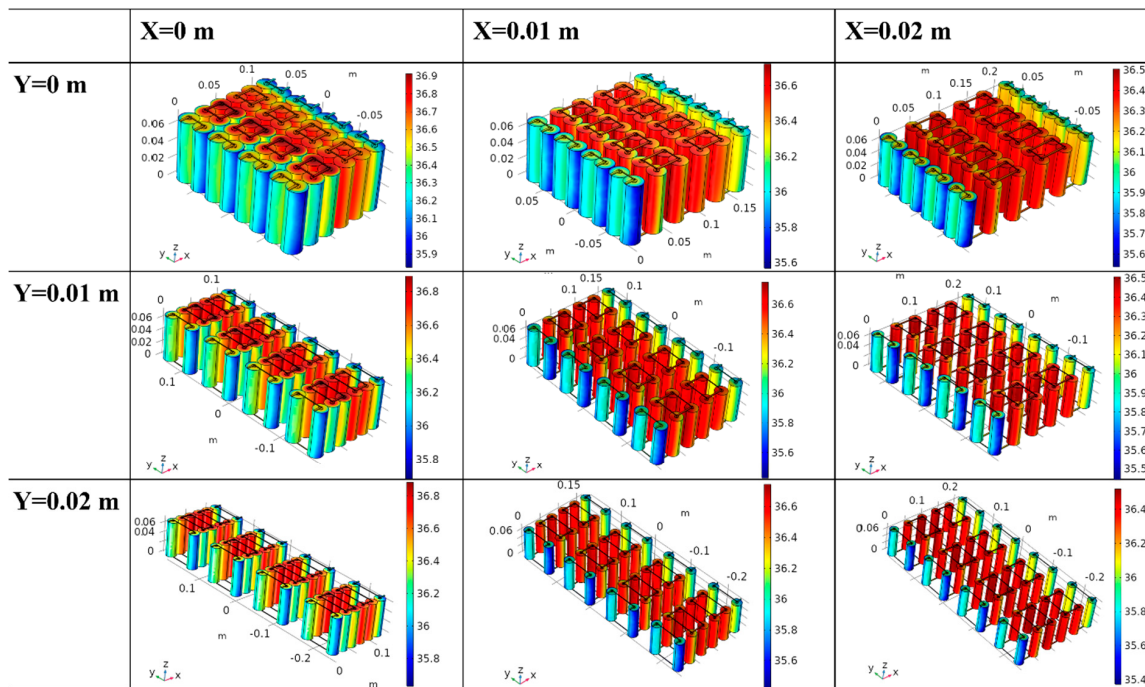


Figure 4. Temperature contours of different battery pack configurations.

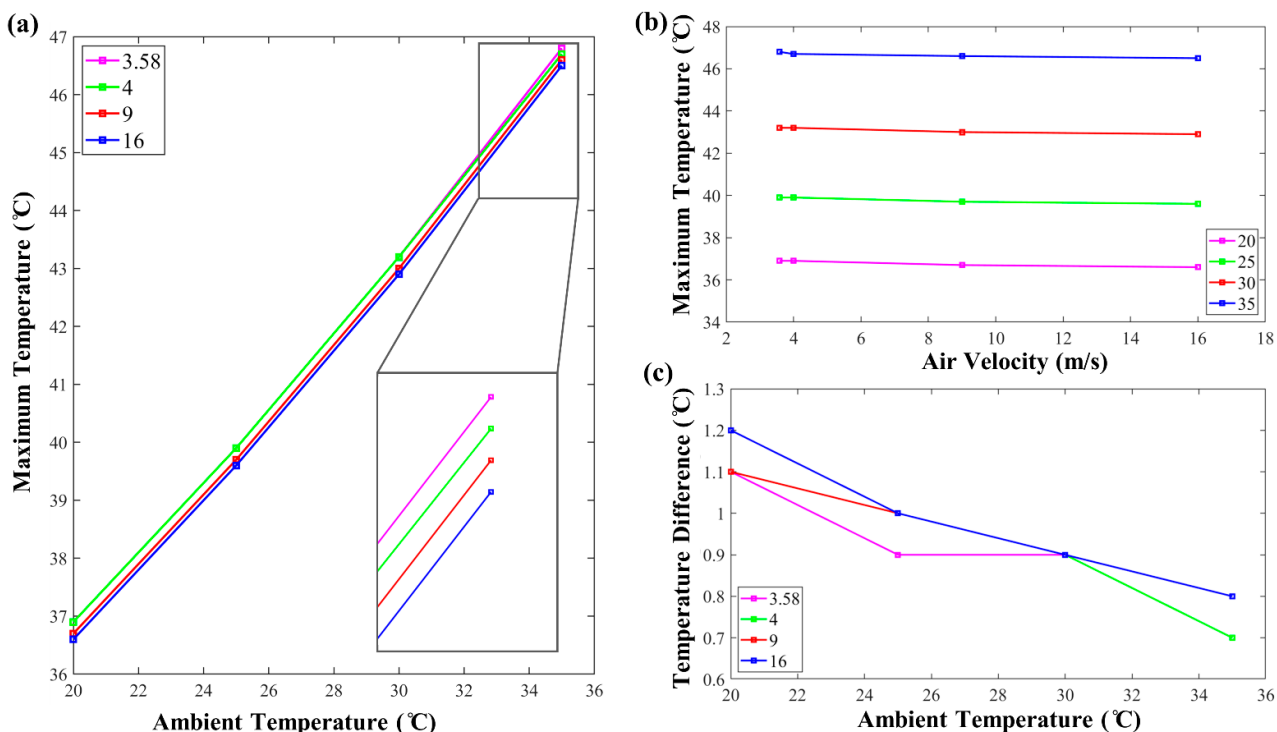


Figure 5. The profile of maximum temperature (a) and temperature difference (b,c) under various operation conditions.

3.2. Training and Results Analysis

In this study, the multilayer perceptron (MLP) neural network was applied. It is one of the most competitive types of ANN for regression in various research fields. Because this approach shows a considerable capability for universal approximation, it is regularly applied to model quite highly complex and disordered phenomena. As mentioned previously, the ANN utilizes the battery thermal distribution simulation dataset obtained through numerical simulations of a typical battery pack configuration on two cylindrical batteries in parallel and six-coupled battery pairs in series. In summary, it consists of 130 data sets of six parameters (four inputs and two outputs) prepared for the training and testing of the ANN. The detailed inputs and outputs of each dataset are illustrated in Table 3. Note that the heat transfer coefficient was replaced with the air velocity more effectively presentative by the ANN. It is possible to extend the ANN model to predictions on other heat transfer methods not considered in the datasets by analyzing their coolant velocity. The heat transfer coefficient of air can be estimated to:

$$h_t = 10.45 - v - 10v^{1/2} \quad (23)$$

where h_t represents the heat transfer coefficient, and v is the relative speed between the object exterior and air. This equation is empirical and can be applied to the velocity range from 2 to 20 m s^{-1} [51].

Table 3. Details of the inputs and outputs for the ANN model.

Parameters	Inputs			Outputs		
	X_Gap	Y_Gap	Air velocity	Ambient temperature	Maximum temperature	Temperature difference
Units	m	m	m s^{-1}	°C	°C	°C
Range	0–0.02	0–0.02	30–39.96	20–30	-	-

The proposed ANN model has been trained using the Levenberg-Marquardt (LM) optimization technique [52]. The LM method based on Levenberg [53] and Marquardt [54] combines Newton's method and gradient descent. It is one of the most efficient training algorithms for neural network modelling [55]. Generally, this algorithm demands more storage space but less time. The training process will be terminated spontaneously when generalization ends improving, as represented by a growth of the mean square error of the validation samples. In the LM method, the Hessian matrix can be approximated as:

$$Hf = Jf^T Jf \quad (24)$$

The gradient is given by:

$$\nabla f = Jf^T e \quad (25)$$

where Jf is the Jacobian matrix and e is the vector of a network error.

The LM working function or the fitness function is based on the mean square error (MSE) between the network output and the target output:

$$F = MSE = \frac{1}{N} \sum_{i=1}^N (R_{i,network} - R_{i,target})^2 \quad (26)$$

where N is the number of datasets, $R_{i,network}$ is the network output and $R_{i,target}$ is the target output from the simulation data. The number of hidden neurons has been mentioned in Equation (22).

Figure 6 demonstrates the ANN regression results, and it plots the regression relation between the physical outputs and the targets, which indicates that this ANN model has achieved a good fit with the training datasets. From Figure 7, the error histogram plot

shows that most errors reside in the range of -0.03688 to 0.0292 . The majority of the predictions had a root mean square (RMS) error of approximately 0.088% , with around 10% of the predictions within $\pm 25\%$ RMS error. The ANN was successfully trained with an overall R (fitness) of 0.999 , with most prediction errors within 1% RMS error. In future works, the ANN model can be further refined to achieve an even higher reliability and accuracy. This can be done by adding more simulation results considering a wider range of configurations or applying more advanced ANN training techniques.

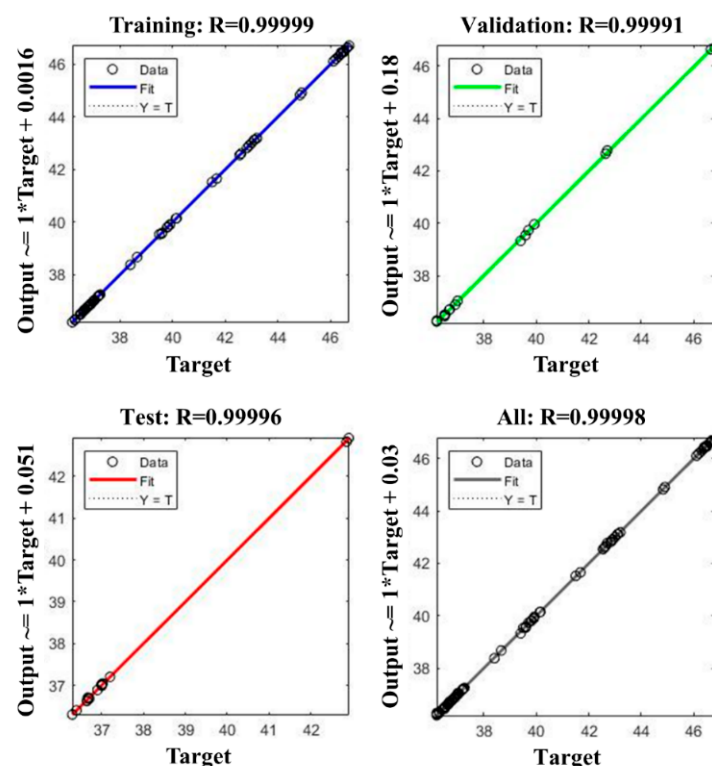


Figure 6. Regression results of ANN model.

3.3. Optimization Analysis and Discussions

The optimization configuration was proposed further to investigate the designed system with various working temperatures to improve the battery system's fire safety performance and cooling efficiency. These simulation results investigated the air velocity and ambient temperature after successfully training the ANN model. A battery pack comprises many single battery cells, and the operation temperature difference for the single battery cell inside the battery pack will be sourced by the temperature imbalance of the battery pack. This will result in the cell's inconsistency, and over the normal state during the charge and discharge process, harm the battery pack service life. Consequently, an appropriate battery thermal management system should simultaneously lower the maximum temperature and temperature difference of the battery packs to ensure the reliability and consistency of EVs and HEVs battery performance.

The 6,250,000 groups of structure and operation features were created in MATLAB. Inputs 1 and 2 are the configuration features, and Inputs 3 and 4 are the operating conditions. The CFD-ANN model calculates the optimal combination to achieve the perfect battery performance under the existing case arrangement with the current four inputs and two outputs.

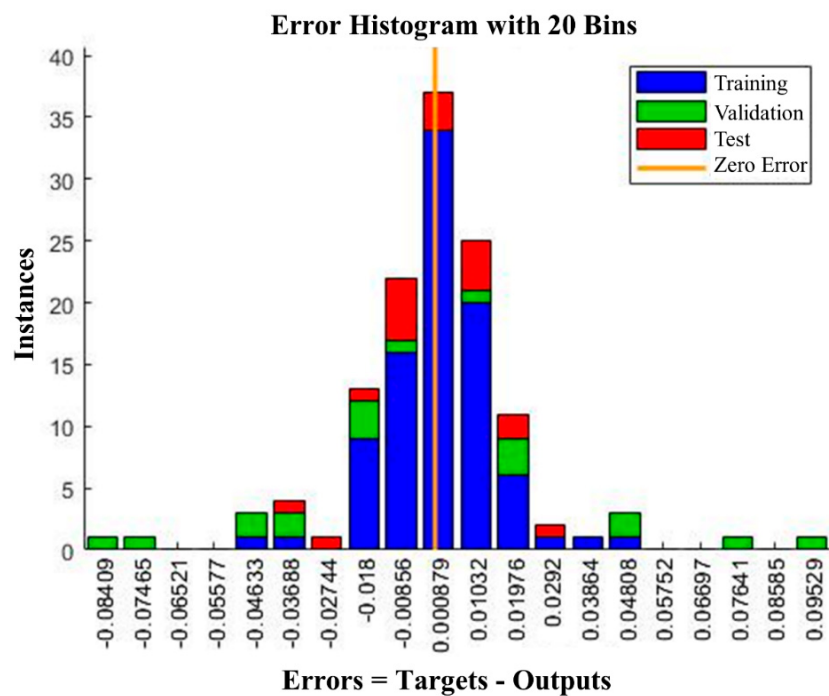


Figure 7. RMS error histogram of the ANN model predictions.

After successful training the ANN model, four inputs were divided into 50 intervals separately in a specific range. Then, 6,250,000 groups of structure features were processed in MATLAB, and the optimal result can be selected. According to Figure 8, the batteries' maximum temperature and temperature difference are greatly affected by the battery configuration and operating conditions, with a fluctuation as high as about 7 °C for the maximum temperature and 1.5 °C for the temperature difference. It can be obtained that the instability of the maximum temperature shows a different trend with the fluctuation of the temperature difference under the current range of various inputs. Therefore, the maximum temperature is chiefly influenced by the battery properties. The temperature difference can be treated as an indicator to evaluate the battery cooling performance of the battery pack.

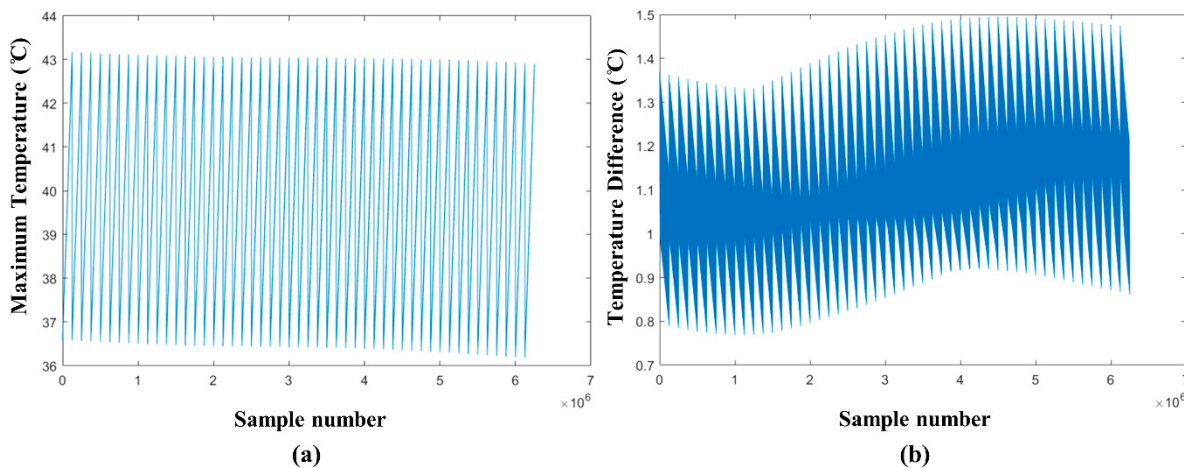


Figure 8. (a) Maximum temperature and (b) temperature difference of the battery pack for different input combinations.

From the CFD-ANN model simulation results, the six million sample results were sorted in ascending order of the battery spacing. Regarding achieving a battery cooling

performance, it can be concluded that the optimal case is the 0.02 m X-direction gap and 0.01 m Y-direction gap under 20 °C ambient temperature and the air velocity 16 m s⁻¹. Compared to the original configuration with the same operating conditions, the maximum temperature decreased by 1.9%, and the temperature difference dropped by 4.5%, which means the CFD-ANN model optimization improved both the cooling efficiency and battery performance. The proposed framework demonstrates an efficient way to improve the thermal performance of the battery pack by optimizing the configuration under different operating conditions.

4. Conclusions

The optimal design of battery thermal management systems was achieved by applying a three-dimensional electro-thermal model coupled with the ANN model. Utilizing numerical simulations via CFD, different battery pack configurations were investigated in a simulation environment to positively impact cooling efficiency, battery performance, and battery fire safety. The three-dimensional electro-thermal model was introduced to calculate the temperature distribution and validated with the previous experimental data. The numerical case studies were applied to train the proposed ANN model, demonstrating the relationship among geometric parameters, operating conditions and cooling efficiency. The CFD-ANN model compared 6,500,000 combinations with various configuration and boundary conditions. The optimal design for the current battery setup was the case with a 0.02 m X-direction gap and a 0.01 m Y-direction gap, which lowered the maximum temperature and temperature difference by 1.9% and 4.5%, respectively.

The results highlighted one significant advantage of numerical simulations. All the pertinent information such as structural parameters and operation requirements can be derived from the model. Furthermore, different factors can be simulated and optimized simultaneously in a simulation environment to deliver a constructive perception of the battery performance and thermal behaviour. In the future, more parameters can be introduced with the current CFD-ANN model, such as electrode materials, electrolyte materials, cell numbers, different coolants, and so forth. A universal database of parameters and repercussions for the battery thermal management system can be prepared, which can then be processed by foresight models to create outlooks and predictions of the fire risks of the LIB energy storage system with a set of input variables.

Author Contributions: Conceptualization, A.L. and A.C.Y.Y.; methodology, A.L. and W.W. (Wei Wang); software, T.B.Y.C.; validation, A.L. and A.C.Y.Y.; formal analysis, A.L. and C.S.L.; investigation, W.W. (Wei Wang); resources, T.B.Y.C. and W.W. (Wei Wu); data curation, W.Y.; writing—original draft preparation, A.L.; writing—review and editing, Q.N.C. and S.K.; visualization, A.L.; supervision, G.H.Y.; project administration, A.C.Y.Y.; funding acquisition, G.H.Y. All authors have read and agreed to the published version of the manuscript.

Funding: This research was funded by the Australian Research Council (ARC Industrial Transformation Training Centre IC170100032) and the Australian Government Research Training Program Scholarship. The authors deeply appreciate all financial and technical supports.

Conflicts of Interest: The authors declare no conflict of interest.

References

1. Yang, Y.; Bremner, S.; Menictas, C.; Kay, M. Battery energy storage system size determination in renewable energy systems: A review. *Renew. Sustain. Energy Rev.* **2018**, *91*, 109–125. [[CrossRef](#)]
2. Armand, M.; Axmann, P.; Bresser, D.; Copley, M.; Edström, K.; Ekberg, C.; Guyomard, D.; Lestriez, B.; Novák, P.; Petranikova, M. Lithium-ion batteries—Current state of the art and anticipated developments. *J. Power Sour.* **2020**, *479*, 228708. [[CrossRef](#)]
3. Li, Y.; Vilathgamuwa, M.; Xiong, B.; Tang, J.; Su, Y.; Wang, Y. Design of minimum cost degradation-conscious lithium-ion battery energy storage system to achieve renewable power dispatchability. *Appl. Energy* **2020**, *260*, 114282. [[CrossRef](#)]
4. Chen, T.; Jin, Y.; Lv, H.; Yang, A.; Liu, M.; Chen, B.; Xie, Y.; Chen, Q. Applications of lithium-ion batteries in grid-scale energy storage systems. *Trans. Tianjin Univ.* **2020**, *26*, 208–217. [[CrossRef](#)]
5. Lai, C.S.; Jia, Y.; Xu, Z.; Lai, L.L.; Li, X.; Cao, J.; McCulloch, M.D. Levelized cost of electricity for photovoltaic/biogas power plant hybrid system with electrical energy storage degradation costs. *Energy Convers. Manag.* **2017**, *153*, 34–47. [[CrossRef](#)]

6. Zhang, C.; Jiang, J.; Gao, Y.; Zhang, W.; Liu, Q.; Hu, X. Charging optimization in lithium-ion batteries based on temperature rise and charge time. *Appl. Energy* **2017**, *194*, 569–577. [[CrossRef](#)]
7. Dong, G.; Wei, J. Determination of the load capability for a lithium-ion battery pack using two time-scale filtering. *J. Power Sour.* **2020**, *480*, 229056. [[CrossRef](#)]
8. Xia, Q.; Wang, Z.; Ren, Y.; Yang, D.; Sun, B.; Feng, Q.; Qian, C. Performance reliability analysis and optimization of lithium-ion battery packs based on multiphysics simulation and response surface methodology. *J. Power Sour.* **2021**, *490*, 229567. [[CrossRef](#)]
9. Feng, X.; Ouyang, M.; Liu, X.; Lu, L.; Xia, Y.; He, X. Thermal runaway mechanism of lithium ion battery for electric vehicles: A review. *Energy Storage Mater.* **2018**, *10*, 246–267. [[CrossRef](#)]
10. Wang, Q.; Mao, B.; Stolarov, S.I.; Sun, J. A review of lithium ion battery failure mechanisms and fire prevention strategies. *Prog. Energy Combust. Sci.* **2019**, *73*, 95–131. [[CrossRef](#)]
11. Sun, P.; Bisschop, R.; Niu, H.; Huang, X. A review of battery fires in electric vehicles. *Fire Technol.* **2020**, *56*, 1–50. [[CrossRef](#)]
12. Li, A.; Yuen, A.C.Y.; Wang, W.; Cordeiro, I.M.d.; Wang, C.; Chen, T.B.Y.; Zhang, J.; Chan, Q.N.; Yeoh, G.H. A Review on Lithium-Ion Battery Separators towards Enhanced Safety Performances and Modelling Approaches. *Molecules* **2021**, *26*, 478. [[CrossRef](#)] [[PubMed](#)]
13. Akinlabi, A.H.; Solyali, D. Configuration, design, and optimization of air-cooled battery thermal management system for electric vehicles: A review. *Renew. Sustain. Energy Rev.* **2020**, *125*, 109815. [[CrossRef](#)]
14. Jiang, Z.; Li, H.; Qu, Z.; Zhang, J. Recent progress in lithium-ion battery thermal management for a wide range of temperature and abuse conditions. *Int. J. Hydrog. Energy* **2022**, *47*, 9428–9459. [[CrossRef](#)]
15. Al-Zareer, M.; Dincer, I.; Rosen, M.A. Novel thermal management system using boiling cooling for high-powered lithium-ion battery packs for hybrid electric vehicles. *J. Power Sour.* **2017**, *363*, 291–303. [[CrossRef](#)]
16. Smith, J.; Singh, R.; Hinterberger, M.; Mochizuki, M. Battery thermal management system for electric vehicle using heat pipes. *Int. J. Therm. Sci.* **2018**, *134*, 517–529. [[CrossRef](#)]
17. Al-Zareer, M.; Dincer, I.; Rosen, M.A. Performance assessment of a new hydrogen cooled prismatic battery pack arrangement for hydrogen hybrid electric vehicles. *Energy Convers. Manag.* **2018**, *173*, 303–319.
18. Saw, L.H.; Ye, Y.; Tay, A.A.; Chong, W.T.; Kuan, S.H.; Yew, M.C. Computational fluid dynamic and thermal analysis of Lithium-ion battery pack with air cooling. *Appl. Energy* **2016**, *177*, 783–792.
19. Kirad, K.; Chaudhari, M. Design of cell spacing in lithium-ion battery module for improvement in cooling performance of the battery thermal management system. *J. Power Sour.* **2021**, *481*, 229016. [[CrossRef](#)]
20. Shen, M.; Gao, Q. A review on battery management system from the modeling efforts to its multiapplication and integration. *Int. J. Energy Res.* **2019**, *43*, 5042–5075. [[CrossRef](#)]
21. Deng, J.; Bae, C.; Marcicki, J.; Masias, A.; Miller, T. Safety modelling and testing of lithium-ion batteries in electrified vehicles. *Nat. Energy* **2018**, *3*, 261–266. [[CrossRef](#)]
22. Cordeiro, I.M.D.C.; Liu, H.; Yuen, A.C.Y.; Chen, T.B.Y.; Li, A.; Cao, R.F.; Yeoh, G.H. Numerical investigation of expandable graphite suppression on metal-based fire. *Heat Mass Transf.* **2021**, *58*, 1–17.
23. Xu, M.; Zhang, Z.; Wang, X.; Jia, L.; Yang, L. Two-dimensional electrochemical–thermal coupled modeling of cylindrical LiFePO₄ batteries. *J. Power Sour.* **2014**, *256*, 233–243. [[CrossRef](#)]
24. Larsson, F.; Anderson, J.; Andersson, P.; Mellander, B.-E. Thermal modelling of cell-to-cell fire propagation and cascading thermal runaway failure effects for lithium-ion battery cells and modules using fire walls. *J. Electrochem. Soc.* **2016**, *163*, A2854. [[CrossRef](#)]
25. Jin, X.; Duan, X.; Jiang, W.; Wang, Y.; Zou, Y.; Lei, W.; Sun, L.; Ma, Z. Structural design of a composite board/heat pipe based on the coupled electro-chemical-thermal model in battery thermal management system. *Energy* **2021**, *216*, 119234. [[CrossRef](#)]
26. Wang, Z.; Fan, W.; Liu, P. Simulation of temperature field of lithium battery pack based on computational fluid dynamics. *Energy Procedia* **2017**, *105*, 3339–3344. [[CrossRef](#)]
27. Wilke, S.; Schweitzer, B.; Khateeb, S.; Al-Hallaj, S. Preventing thermal runaway propagation in lithium ion battery packs using a phase change composite material: An experimental study. *J. Power Sour.* **2017**, *340*, 51–59. [[CrossRef](#)]
28. An, Z.; Jia, L.; Li, X.; Ding, Y. Experimental investigation on lithium-ion battery thermal management based on flow boiling in mini-channel. *Appl. Therm. Eng.* **2017**, *117*, 534–543. [[CrossRef](#)]
29. Ouyang, D.; Liu, J.; Chen, M.; Weng, J.; Wang, J. An experimental study on the thermal failure propagation in lithium-ion battery pack. *J. Electrochem. Soc.* **2018**, *165*, A2184. [[CrossRef](#)]
30. Li, H.; Duan, Q.; Zhao, C.; Huang, Z.; Wang, Q. Experimental investigation on the thermal runaway and its propagation in the large format battery module with Li (Ni1/3Co1/3Mn1/3)O₂ as cathode. *J. Hazard. Mater.* **2019**, *375*, 241–254. [[CrossRef](#)]
31. Zhang, X.; Wang, Y.; Wu, J.; Chen, Z. A novel method for lithium-ion battery state of energy and state of power estimation based on multi-time-scale filter. *Appl. Energy* **2018**, *216*, 442–451. [[CrossRef](#)]
32. Li, K.; Yan, J.; Chen, H.; Wang, Q. Water cooling based strategy for lithium ion battery pack dynamic cycling for thermal management system. *Appl. Therm. Eng.* **2018**, *132*, 575–585. [[CrossRef](#)]
33. Zhao, R.; Zhang, S.; Liu, J.; Gu, J. A review of thermal performance improving methods of lithium ion battery: Electrode modification and thermal management system. *J. Power Sour.* **2015**, *299*, 557–577. [[CrossRef](#)]
34. Kim, J.; Oh, J.; Lee, H. Review on battery thermal management system for electric vehicles. *Appl. Therm. Eng.* **2019**, *149*, 192–212. [[CrossRef](#)]

35. Patel, J.R.; Rathod, M.K. Recent developments in the passive and hybrid thermal management techniques of lithium-ion batteries. *J. Power Sour.* **2020**, *480*, 228820. [[CrossRef](#)]
36. Fan, L.; Khodadadi, J.; Pesaran, A. A parametric study on thermal management of an air-cooled lithium-ion battery module for plug-in hybrid electric vehicles. *J. Power Sour.* **2013**, *238*, 301–312. [[CrossRef](#)]
37. Wang, T.; Tseng, K.; Zhao, J.; Wei, Z. Thermal investigation of lithium-ion battery module with different cell arrangement structures and forced air-cooling strategies. *Appl. Energy* **2014**, *134*, 229–238. [[CrossRef](#)]
38. Choudhari, V.; Dhoble, A.; Panchal, S. Numerical analysis of different fin structures in phase change material module for battery thermal management system and its optimization. *Int. J. Heat Mass Transf.* **2020**, *163*, 120434. [[CrossRef](#)]
39. Chen, S.; Peng, X.; Bao, N.; Garg, A. A comprehensive analysis and optimization process for an integrated liquid cooling plate for a prismatic lithium-ion battery module. *Appl. Therm. Eng.* **2019**, *156*, 324–339. [[CrossRef](#)]
40. Mitchell, T.M. *Machine Learning*; McGraw-hill: New York, NY, USA, 1997.
41. Jalilantabar, F.; Mamat, R.; Kumarasamy, S. Prediction of lithium-ion battery temperature in different operating conditions equipped with passive battery thermal management system by artificial neural networks. *Mater. Today Proc.* **2022**, *48*, 1796–1804. [[CrossRef](#)]
42. Wu, B.; Han, S.; Shin, K.G.; Lu, W. Application of artificial neural networks in design of lithium-ion batteries. *J. Power Sour.* **2018**, *395*, 128–136. [[CrossRef](#)]
43. Qian, X.; Xuan, D.; Zhao, X.; Shi, Z. Heat dissipation optimization of lithium-ion battery pack based on neural networks. *Appl. Therm. Eng.* **2019**, *162*, 114289. [[CrossRef](#)]
44. Feng, F.; Teng, S.; Liu, K.; Xie, J.; Xie, Y.; Liu, B.; Li, K. Co-estimation of lithium-ion battery state of charge and state of temperature based on a hybrid electrochemical-thermal-neural-network model. *J. Power Sour.* **2020**, *455*, 227935. [[CrossRef](#)]
45. Shi, Y.; Ahmad, S.; Liu, H.; Lau, K.T.; Zhao, J. Optimization of air-cooling technology for LiFePO₄ battery pack based on deep learning. *J. Power Sour.* **2021**, *497*, 229894. [[CrossRef](#)]
46. Guo, M.; Sikha, G.; White, R.E. Single-particle model for a lithium-ion cell: Thermal behavior. *J. Electrochem. Soc.* **2010**, *158*, A122. [[CrossRef](#)]
47. Doyle, M.; Newman, J.; Gozdz, A.S.; Schmutz, C.N.; Tarascon, J.M. Comparison of modeling predictions with experimental data from plastic lithium ion cells. *J. Electrochem. Soc.* **1996**, *143*, 1890. [[CrossRef](#)]
48. Chen, S.-C.; Wang, Y.-Y.; Wan, C.-C. Thermal analysis of spirally wound lithium batteries. *J. Electrochem. Soc.* **2006**, *153*, A637. [[CrossRef](#)]
49. Chen, M.; Challita, U.; Saad, W.; Yin, C.; Debbah, M. Artificial neural networks-based machine learning for wireless networks: A tutorial. *IEEE Commun. Surv. Tutor.* **2019**, *21*, 3039–3071. [[CrossRef](#)]
50. Hunter, D.; Yu, H.; Pukish, M.S., III; Kolbusz, J.; Wilamowski, B.M. Selection of proper neural network sizes and architectures—A comparative study. *IEEE Trans. Ind. Inform.* **2012**, *8*, 228–240. [[CrossRef](#)]
51. ToolBox, E. Convective Heat Transfer. Available online: https://www.engineeringtoolbox.com/convective-heat-transfer-d_430.html (accessed on 27 July 2021).
52. Hagan, M.T.; Menhaj, M.B. Training feedforward networks with the Marquardt algorithm. *IEEE Trans. Neural Netw.* **1994**, *5*, 989–993. [[CrossRef](#)]
53. Levenberg, K. A method for the solution of certain non-linear problems in least squares. *Q. Appl. Math.* **1944**, *2*, 164–168. [[CrossRef](#)]
54. Marquardt, D.W. An algorithm for least-squares estimation of nonlinear parameters. *J. Soc. Ind. Appl. Math.* **1963**, *11*, 431–441. [[CrossRef](#)]
55. Yetik, O.; Karakoc, T.H. Estimation of thermal effect of different busbars materials on prismatic Li-ion batteries based on artificial neural networks. *J. Energy Storage* **2021**, *38*, 102543. [[CrossRef](#)]